Evolution of Shell Nonuniformities near Peak Compression of a Spherical Implosion

V. A. Smalyuk, V. N. Goncharov, J. A. Delettrez, F. J. Marshall, D. D. Meyerhofer,* S. P. Regan, and B. Yaakobi

Laboratory for Laser Energetics, University of Rochester, 250 East River Road, Rochester, New York 14623

(Received 4 April 2001; published 25 September 2001)

The evolution of shell modulations near peak compression of direct-drive spherical-target implosions has been measured using the 60-beam, 30-kJ UV OMEGA laser system. The spatial size and amplitude of shell-areal-density modulations decrease during the target compression, then increase during its decompression as expected. The shell uniformity at peak compression has been increased by reducing single-beam, laser-drive nonuniformity.

DOI: 10.1103/PhysRevLett.87.155002 PACS numbers: 52.35.Py, 52.50.Jm, 52.70.La

In inertial confinement fusion (ICF), a spherical target is imploded by either direct illumination of laser beams (direct drive) [1] or x rays produced in high-Z enclosure (hohlraum) [2]. Target perturbations can be amplified by hydrodynamic instabilities to disrupt the implosion and degrade target performance. Such perturbations result from target imperfections and drive nonuniformities, including imprinted modulations from laser nonuniformities in the case of direct-drive ICF. The unstable growth of target perturbations has been extensively studied in planar geometry with preimposed modulations using indirect drive [3,4] and both preimposed and imprinted modulations using direct drive [5–8]. Experiments in cylindrical [9] and spherical [10] geometry have studied effects of convergence on the unstable growth. The modulation growth is typically measured by backlighting the driven target with x rays [11]. The backlighter x rays are attenuated while passing through the target, allowing measurements of the target-areal-density modulations.

Near peak compression of a spherical-target implosion, when the maximum density and temperature occur, the hot, compressed core and inner surface of the shell produce strong x-ray emission. This emission can be used as a backlighter to probe the outer, colder shell [12]. The first shell-integrity measurements, based on this method, were time integrated over the duration of peak compression (~200 to 300 ps) of the implosion [12,13]. They used shells with titanium-doped layers and imaging at photon energies above and below the titanium K edge. Core images at photon energies below the K edge (not absorbed by the shell) provide the spatial shape of the backlighter, while core images at photon energies above the K edge (highly absorbed by the shell's titanium) contain information about the structure of shell-areal-density modulations in the titanium-doped layer. The experiment described in this Letter, based on the techniques developed in time-integrated experiments [12,13], is the first measurement of the evolution of shell nonuniformities near peak compression of a spherical-target implosion using targets with titanium-doped layers. The growth of shell modulations in the deceleration phase is measured for the first time in ICF implosion experiments. The core emission, temperature, and shell-areal-density histories are also measured. Areal-density modulations in a titanium-doped layer have been determined from the intensity ratios of time-resolved 2D core images taken above and below the titanium K edge. The average areal density has been measured using streak spectroscopy of titanium absorption of core radiation above the titanium K edge.

Spherical targets with an initial diameter of about 920 μm filled with 15 atm of D_2 gas were imploded using direct-drive, 351-nm laser illumination on the 60-beam OMEGA laser system [14]. The pulse shape was a 1-ns square with total on-target energy of about 23 kJ. The target shells had inner 1.9-μm-thick, titanium-doped (6% by atom) CH layers, and outer, about 18-μm-thick, pure-CH layers. Initial areal density of titanium in the shell was about 0.05 mg/cm^2. All laser beams were smoothed with distributed phase plates (DPP's) [15], 1-THz two-dimensional smoothing by spectral dispersion (2D SSD) [16], and polarization smoothing (PS) [17] using birefringent wedges. The average beam-to-beam energy imbalance was about 3.8%. The target emission was imaged on a four-strip framing camera [18,19] by a 6-μm-diam pinhole array, protected by a 200-μm-thick beryllim filter. The upper two strips of the framing camera were filtered with 75-μm-thick titanium filter, and the lower two strips by a 50-μm-thick iron filter to image core radiation at photon energies below (~4.8 keV) and above (~6.5 keV) the titanium K edge (4.966 keV), simultaneously [19]. The two x-ray energy channels had spectral bandwidths ($\Delta E/E$) of about 20%. Each image taken with the framing camera had a temporal resolution of ~40 ps and a spatial resolution of about 6 μm. The framing camera output was captured on a charge-coupled-device camera with a 9-μm pixel size [20] and a magnification of 12.

The spectral evolution of core emission was captured on an x-ray streak camera [21] with a temporal resolution of ~20 ps. The streaked spectrum was calibrated by a time integrated spectrum measured with an ammonium di-hydrogen phosphate crystal. Figure 1 shows a spectral evolution of core emission as a function of photon energy near peak compression (~2.0 ns) for one of the three similar shots, integrated over the core size for times 1.77, 1.82, and 1.92 ns [Fig. 1(a)] and 1.97, 2.02, and 2.07 ns

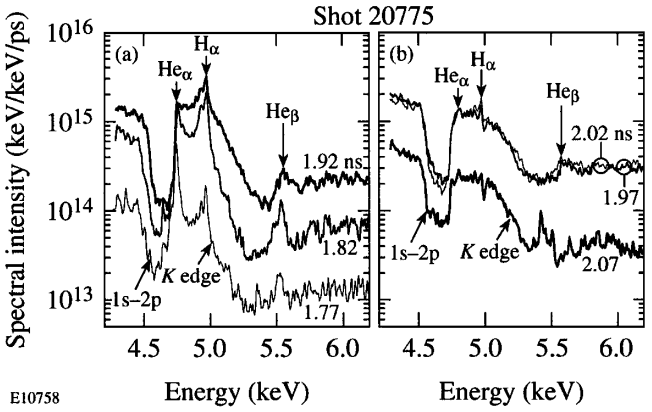

FIG. 1. Evolution of core emission spectral intensity as a function of photon energy for times 1.77, 1.82, 1.92, 1.97, 2.02, and 2.07 ns near peak compression of the spherical implosion.

[Fig. 1(b)]. Core images for the same 6 times captured with the framing camera (in the same shot 20 775) are shown in Fig. 2, with the upper six images corresponding to the photon energy channel below the titanium K edge, and the lower six images to the channel above the K edge. These images have each been normalized to their highest intensities. The measured spectra (shown in Fig. 1) contain information about (i) evolution of Heα, Hα, and Heβ line emission of titanium ions mixed with the core fuel, (ii) $1s$-$2p$ absorption lines (near ~4.6 keV) of warm titanium with temperatures $T \sim 500$ and 700 eV in the shell, (iii) absorption above the K edge (at 4.966 keV) of cold titanium ($T < 500$ eV) in the shell [12,13], and (iv) hot core continuum emission. The effective electron temperature in the emission region T_e and average cold titanium areal density has been calculated by fitting the function $I(E) = I_0 e^{\{-E/T_e - \mu_{\rm Ti}(E)\cdot[\rho d]_{\rm Ti}\}}$ to the measured spectra (outside of the absorption area of warm titanium near ~4.6 keV, and the shifting K edge), where E is the photon energy, $\mu_{\rm Ti}(E)$ and $[\rho d]_{\rm Ti}$ are the cold titanium mass absorption coefficient and average areal density, respectively, and I_0 is the constant. The effect of CH absorption was negligible compared to titanium absorption in these experiments because all time-resolved images below and above the K edge were always identical within experimental noise in shots with CH-only shells (containing no titanium) taken at similar drive conditions. Figure 3 shows a temporal evolution of the electron temperature T_e of the core and the shell-emitting regions [open circles connected by a thin solid line in Fig. 3(a)] and areal density of the cold titanium in the shell $[\rho d]_{\rm Ti}$ [closed triangles connected by a thin solid line in Fig. 3(b)]. The measured areal density of titanium has been normalized to the initial titanium areal density of the undriven target and represents the amount of compression in the layer. The thick solid lines in Figs. 3(a) and 3(b) show the evolution of continuum emission intensity in arbitrary units at photon energies of 4.8 to 4.9 keV below the titanium K edge, calculated using core emission spectra measured with the streak camera. The closed squares in Figs. 3(a) and 3(b) show intensity (in arbitrary units) evolution for the six images (Fig. 2) measured with the framing camera, also below the titanium K edge.

The modulations in the cold, or absorbing, part of the shell areal density $\delta[\rho d](\mathbf{r}, t)$ at time t ($\mathbf{r}$ is the spatial coordinate) are proportional to the modulation in the logarithm of the ratio of intensities of the two images at photon energies above (highly absorbing by the shell) $I_{>K}(\mathbf{r}, t)$ and below (weakly absorbing by the shell) the titanium K edge, $I_{<K}(\mathbf{r}, t)$:

$$\delta[\rho d](\mathbf{r}) = \frac{\delta\{\ln[I_{<K}(\mathbf{r})/I_{>K}(\mathbf{r})]\}}{(\mu_{>K} - \mu_{<K})}, \qquad (1)$$

where $\mu_{>K} = 0.37 \pm 0.02$ cm^2/mg and $\mu_{<K} = 0.11 \pm 0.02$ cm^2/mg are the spectrally weighed mass absorption coefficients of cold titanium at photon energies above and below the K edge, respectively [13]. The absorption coefficients have been calculated for each time t using the measured x-ray spectra shown in Fig. 1 and filter functions of beryllium, titanium, and iron filters [13]. Images $I_{<K}(\mathbf{r}, t)$ and $I_{>K}(\mathbf{r}, t)$ have been obtained from "raw" images (shown in Fig. 2) using the Wiener-filtering technique) [13,19], which was based on the measured system resolution (~6 μm) [19] and the system noise (determined by the photon statistics of core x rays) [19]. All approximations and assumptions made in deriving Eq. (1) have been presented and discussed in detail in Refs. [12,13,19].

Figure 4(a) shows the evolution of areal-density modulations calculated using core images at 1.92, 1.97, 2.02, and 2.07 ns, shown in Fig. 2 and Eq. (1), and normalized to their measured (with the streak camera) averaged areal densities, shown in Fig. 3(b). The images at early times 1.77 and 1.82 ns do not have sufficient backlighter area (first two images at the ~4.8-keV channel) to probe the nonuniformities in the cold shell. The spatial scale of modulations decreases from time 1.92 ns to time 2.02 ns (as evident from the motion of the red "circular" structure in corresponding images), and then shorter-scale modulations start to grow in the image at 2.07 ns. The image size at 2.07 ns is smaller than images at early times because the level of backlighter emission drops late in the implosion. The effect of titanium line emission on the spatial shape of images below the K edge was negligible because core images, routinely measured with a pinhole-array spectrometer [12], had always the same spatial shapes at photon energies of titanium (Heα, Hα) lines and photon energies outside these lines below the K edge. The minimum level of modulations with $\sigma_{\rm rms} = (18 \pm 8)\%$ occurs near 2.0 ns. The modulation $\sigma_{\rm rms}$ decreases by about 20% from time 1.92 ns to time 2.02 ns, when the maximum core emission intensity and temperature occur (see Fig. 3); then it grows by about 60% during decompression while emission intensity and temperature drop.

The shell modulation level at peak compression depends on the initial modulation level at the beginning of implosion and the amount of unstable growth during

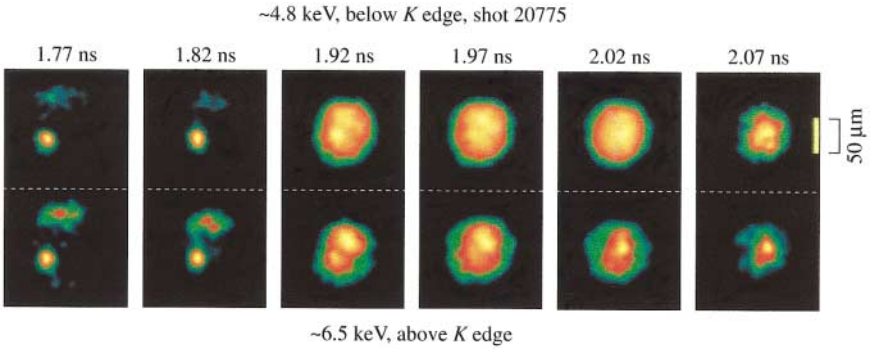

FIG. 2 (color). "Raw" core images near peak compression at energies below (~4.8 keV, upper row of images) and above (~6.5 keV, lower row of images) the titanium K edge for times 1.77, 1.82, 1.92, 1.97, 2.02, and 2.07 ns.

implosion. The initial target modulations come primarily from the imprinting [5–8] of laser beam nonuniformities in direct-drive ICF. Beam-smoothing techniques such as DPP's [15], SSD [16], and PS [17] are applied on OMEGA [14] to minimize initial target modulations. To check the sensitivity of shell modulations at peak compression to the initial target modulations, we compare two implosions with similar targets and drive conditions but with different levels of beam smoothing; one shot was taken at the best smoothing conditions, including 1 THz, 2D SSD, and PS; the other shot had a 3-color-cycle, 0.35 THz, 2D SSD, and no PS. Figure 4(b) compares minimum levels of shell modulations near peak compression for these two shots. The level of shell modulations is significantly higher with less-uniform drive using 0.35-THz SSD and no PS [$\sigma_{\mathrm{rms}} = (43 \pm 12)\%$] than with 1-THz SSD and PS [$\sigma_{\mathrm{rms}} = (18 \pm 9)\%$]. Implosions driven with more-uniform beams (1-THz SSD and PS) have primary neutron yields and fuel areal densities ~70% higher than with 0.35-THz SSD and no PS [22].

A spherical implosion postprocessor [23] to 1D hydrocode LILAC [24] was applied to qualitatively explain the experimental data. This postprocessor uses a sharp-boundary model to study the perturbation evolution in the shell. During the acceleration phase of implosion, when the shell is driven by the laser beams, the shell nonuniformities grow due to the Rayleigh-Taylor (RT) instability [2–10]. When the 1-ns laser drive is turned off, the shell slows down while converging inward to the target center, stops at stagnation, and then moves outward. Since the higher-density shell is slowed down by the lower-density D_2 gas, the inner surface of the shell is subject to the RT instability during the deceleration phase. The shell-areal-density modulation (the quantity measured in the experiment) can be written in the following form: $\delta(\rho d) \approx \rho\eta_f + \rho\eta_b$, where ρ is the average shell density, η_f and η_b are the amplitudes on the front- and back-surface distortions, and d is the shell thickness. During the shell acceleration, when the front surface is RT unstable, the first term, $\rho\eta_f$, gives the dominant contribution to $\delta(\rho d)$. In addition, the front-surface perturbations feed through the shell ($\eta_b \sim \eta_f e^{-kd}$, where k is the modulation wave number), seeding the deceleration-phase RT instability on the inner surface. After the laser is turned off and the shell starts to decelerate, the ablation front becomes stable and perturbation η_f oscillates. One can estimate the period of such

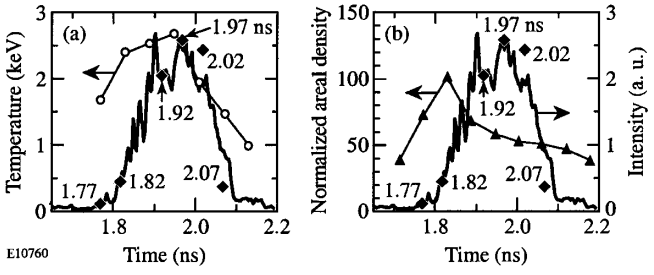

FIG. 3. (a) Evolution of core continuum emission temperature (open circles), core continuum emission intensity (at 4.8 to 4.9 keV, thick solid line), and emission intensity in images below the K edge (solid squares) for the same times at in Fig. 2. (b) Evolution of normalized areal density of titanium (closed triangles) together with core continuum emission intensity and emission intensity in images below the K edge from (a).

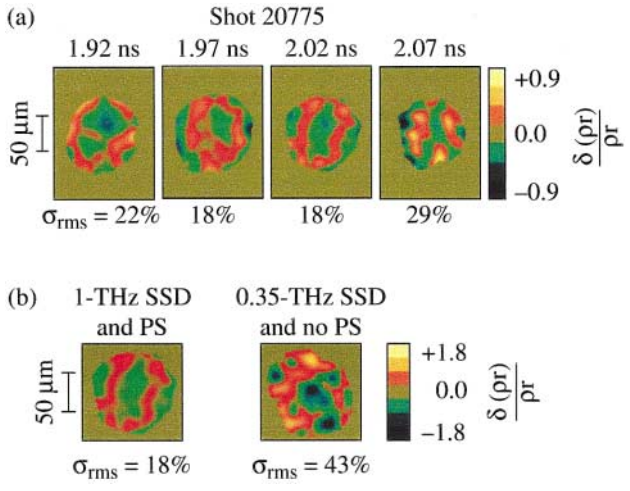

FIG. 4 (color). (a) Normalized areal-density modulations at 1.92, 1.97, 2.02, and 2.07 ns for shot 20 775. (b) Normalized areal-density modulations for two shots: one with 1-THz SSD and PS from (a) at 2.02 ns, the other with 3-color-cycle, 0.35-THz SSD, and no PS at peak compression.

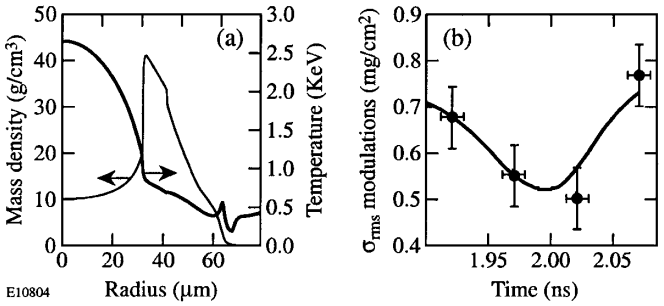

FIG. 5. (a) The simulated profiles of target density and temperature during the deceleration phase of the implosion. (b) The evolution of titanium areal-density modulations in the shell calculated by the model (solid line) and measured (closed circles).

oscillations $T \sim 2\pi\sqrt{R/(\ell g)}$, where $R \approx 60$ μm is the shell radius, ℓ is the mode number, and $g \approx 10^3$ μm/ns is the deceleration. Substituting results of the 1D LILAC [24] simulation to the above formula gives $T = 600$ ps for the dominant in the experiment mode $\ell = 6$ (which corresponds to a modulation wavelength of about 60 μm). Therefore, during the time of measurement $\Delta t = 300$ ps, the front-surface modulation changes its sign. Thus, there are two competing effects: first, the reduction of front-surface modulations $\eta_f \sim \eta_0 \cos(2\pi t/T)$ due to phase change, and, second, an increase in back-surface modulations $\eta_b \sim \eta_0 \exp(\gamma t - kd)$ due to the RT growth, where γ is the instability growth rate. Initially, $\eta_f > \eta_b$, and the reduction in the front-surface amplitude leads to the reduction in the areal-mass modulation. Later, when η_b becomes dominant, growth in shell-areal-density modulation $\delta(\rho d)$ is caused by the exponential growth of the back-surface modulation. In addition to the described effect, an additional reduction in cold $\delta(\rho d)$ could be due to the heating of the inner titanium-doped layer of the shell.

Figure 5(a) shows the profiles of target density and temperature in the deceleration phase of the implosion at peak compression (simulated by the 1D code LILAC). The bulk of the shell is dense and relatively cold with an electron temperature less than 1 keV, while the core is hotter and less dense. The solid line in Fig. 5(b) shows the evolution of shell-areal-density modulations calculated with the model for the dominant mode $\ell = 6$ based on the 1D LILAC simulation. The modulations of total shell areal density $\delta(\rho d)$ decrease, while they are dominated by sinusoidally decreasing modulations at the outer surface. When exponentially growing modulations at the inner surface become higher than outer-surface modulations, the total shell-areal-density modulations grow. The circles in Fig. 5(b) show than $\sigma_{\rm rms}$ of measured shell-areal-density modulations [shown in Fig. 4(a)] follows well the model prediction. The results of the model were normalized to the experimental point at $t = 1.97$ ns. The experimental points have been averaged using data from three shots taken at similar conditions. Since the measured spectrum of shell-areal-density modulations is located in the vicinity of the model $\ell = 6$ (similar to previous time-integrated measurements [12,13]), the comparison of measured modulation $\sigma_{\rm rms}$ with the calculated amplitude of the dominant spectral mode becomes qualitatively reasonable.

This Letter has presented the evolution of shell modulations near peak compression of a spherical implosion. The minimum level of areal-density modulations, with $\sigma_{\rm rms} = 18\%$ occurs at the peak of core emission with a laser drive that included 1-THz SSD and PS. In lower laser beam uniformity implosions with 3-color-cycle, 0.35-THz SSD and no PS, the level of modulations was significantly higher, with $\sigma_{\rm rms} = 43\%$. The level of measured shell-areal-density modulations decreases while it is dominated by the decreasing modulations at the stable outer surface, then increases when it is dominated by growing modulations at the unstable inner surface, as expected.

This work was supported by the U.S. Department of Energy Office of Inertial Confinement Fusion under Cooperative Agreement No. DE-FC03-92SF19460, the University of Rochester, and the New York State Energy Research and Development Authority. The support of DOE does not constitute an endorsement by DOE of the views expressed in this article.

*Also at Departments of Mechanical Engineering, and Physics and Astronomy.

[1] J. H. Nuckolls *et al.,* Nature (London) **239**, 139 (1972).
[2] J. D. Lindl, Phys. Plasmas **2**, 3933 (1995).
[3] S. G. Glendinning *et al.,* Phys. Rev. Lett. **78**, 3318 (1997).
[4] M. M. Marinak *et al.,* Phys. Rev. Lett. **80**, 4426 (1998).
[5] C. J. Pawley *et al.,* Phys. Plasmas **6**, 565 (1999).
[6] H. Azechi *et al.,* Phys. Plasmas **4**, 4079 (1997).
[7] R. J. Taylor *et al.,* Phys. Rev. Lett. **76**, 1643 (1996).
[8] D H. Kalantar *et al.,* Phys. Plasmas **4**, 1985 (1997).
[9] D. L. Tubbs *et al.,* Phys. Plasmas **6**, 2095 (1999).
[10] S. D. Glendinning *et al.,* Phys. Plasmas **7**, 2033 (2000).
[11] S. G. Glendinning *et al.,* in *Laser Plasma Diagnostics of Dense Plasmas,* edited by M. C. Richardson and G. A. Kyrala, SPIE Proceedings Vol. 2523 (SPIE–International Society for Optical Engineering, Bellingham, WA, 1995), pp. 29–39.
[12] B. Yaakobi *et al.,* Phys. Plasmas **7**, 3727 (2000).
[13] V. A. Smalyuk *et al.,* Phys. Plasmas **8**, 2872 (2001).
[14] T. R. Boehly *et al.,* Opt. Commun. **133**, 495 (1997).
[15] Y. Lin, T. J. Kessler, and G. N. Lawrence, Opt. Lett. **20**, 764 (1995).
[16] S. P. Regan *et al.,* J. Opt. Soc. Am. B **17**, 1483 (2000).
[17] T. R. Boehly *et al.,* J. Appl. Phys. **85**, 3444 (1999).
[18] C. J. Pawley *et al.,* Rev. Sci. Instrum. **71**, 1286 (2000).
[19] V. A. Smalyuk *et al.,* Rev. Sci. Instrum. **72**, 635 (2001).
[20] R. E. Turner *et al.,* Rev. Sci. Instrum. **72**, 706 (2001).
[21] D. H. Kalantar *et al.,* Rev. Sci. Instrum. **72**, 751 (2001).
[22] D. D. Meyerhofer *et al.,* Phys. Plasmas **8**, 2251 (2001).
[23] V. N. Goncharov *et al.,* Phys. Plasmas **7**, 5118 (2000).
[24] J. Delettrez and E. B. Goldman, Phys. Rev. A **36**, 3926 (1987).